

# Accelerated Bayesian optimization in deep cooling atoms

Changwen Liang<sup>1,2,†</sup>, Jun Yang<sup>1,2,†,\*</sup>, Rong Sha<sup>1,2,†</sup>, Xiaoxiao Ma<sup>1,2,†</sup>, Chao Zhou<sup>1,2</sup>, Qixue Li<sup>1,2</sup>, Guochao Wang<sup>1,2</sup>, Jixun Liu<sup>1,2</sup>, Shuhua Yan<sup>1,2,\*</sup>, Lingxiao Zhu<sup>1,2,\*</sup>

<sup>1</sup> College of Intelligence Science and Technology, National University of Defense Technology, Changsha 410073, China

<sup>2</sup> Interdisciplinary Center for Quantum Information, National University of Defense Technology, Changsha, 410073, China

\* Corresponding author. Email: jyang@nudt.edu.cn (J.Y.); yanshuhua996@163.com (S.Y.); zhulingxiao31@163.com (L.Z.).

<sup>†</sup>These authors contributed equally to this work.

## Abstract

Laser cooling, which cools atomic and molecular gases to near absolute zero, is the crucial initial step for nearly all atomic gas experiments. However, fast achievement of numerous sub- $\mu\text{K}$  cold atoms is challenging. To resolve the issue, we propose and experimentally validate an intelligent polarization gradient cooling approach enhanced by optical lattice, utilizing Maximum Hypersphere Compensation Sampling Bayesian Optimization (MHCS-BO). MHCS-BO demonstrates a twofold increase in optimization efficiency and superior prediction accuracy compared to conventional Bayesian optimization. Finally, approximate  $10^8$  cold atoms at a temperature of  $0.4 \pm 0.2 \mu\text{K}$  can be achieved given the optimal parameters within 15 minutes. Our work provides an intelligent protocol, which can be generalized to other high-dimension parameter optimization problems, and paves way for preparation of ultracold atom in quantum experiments.

## Introduction

Atomic cooling plays a crucial role in various quantum systems, including quantum precision measurement (1–4), quantum simulation (5–7), and quantum information (8–10). Atomic cooling methods include magneto-optical trap (MOT) cooling (11), polarization gradient cooling (PGC) (12), evaporation cooling (13), Raman sideband cooling (14) and so on. Among these, PGC stands out as a cheap approach that could obtain lower atomic temperature simply by designing timing sequence without the need for extra hardware. The stand PGC can usually obtain cold atoms at  $\mu\text{K}$  level. With the aid of optical lattice to adiabatic cooling, the atomic temperature could be further reduced (15). However, the process of preparing cold atoms is quite complex, highly nonlinear, and susceptible to environmental influences. Conventional manual optimization results in low accuracy and efficiency, making it difficult to control the cooling process more finely due to the complexities associated of high-dimension optimization. It is also particularly challenging to ensure a lower temperature while maintaining a higher atom number.

Recently, artificial intelligence (AI) has been applied to solve optimization problems involving quantum systems (16–18). Evolutionary algorithm such as genetic algorithm (19), differential evolution (20), particle swarm optimization (21), can search global optimal parameters. However, these algorithms, usually depending on large population scale and iteration steps, work inefficiently in scenarios with high experimental cost. Neural networks (NNs) such as multi-layer perceptron (22), deep learning (23, 24), reinforcement learning (25, 26) are applicable to high-dimensional multi-objective optimization problems. Similar to Evolutionary algorithm, NNs also require a large amount of experimental data to train networks. The accuracy of NNs extremely requires robust system and high-quality datasets. Fortunately, Bayesian optimization (BO) (27, 28) can efficiently optimize parameters

especially in complex systems with high experimental cost. The acquisition function, e.g., expected improvement (EI), probability of improvement and upper confidence bound, could obtain good optimization effects in the majority of scenarios. Nevertheless, the traditional acquisition functions always leave large non-sampling regions in parameter space, compromising the predictive performance of the model in high dimension.

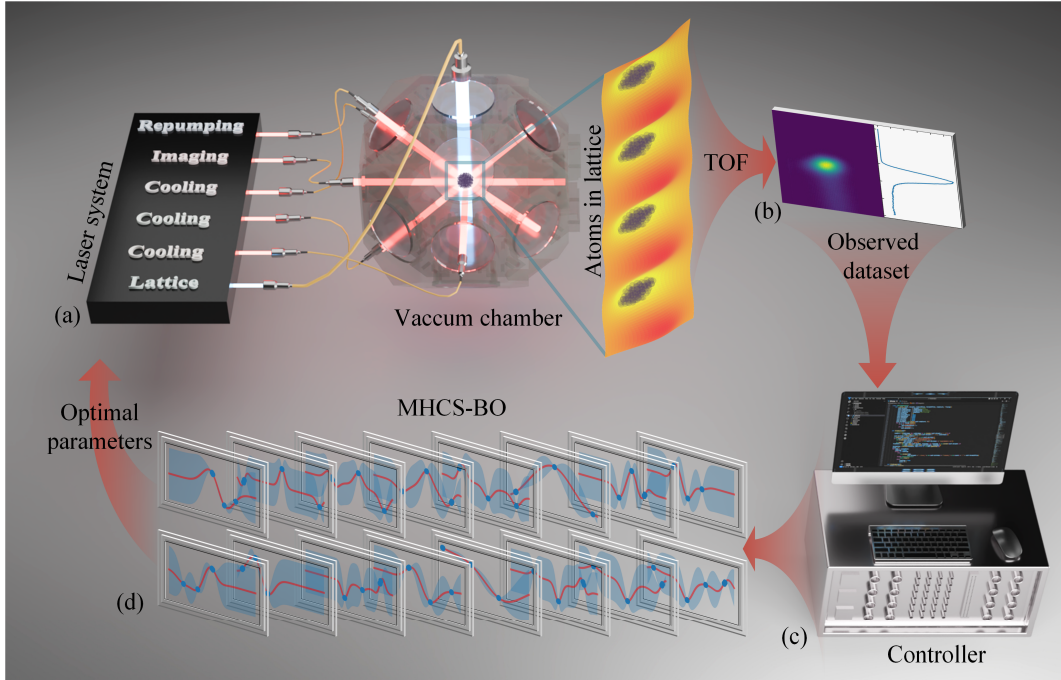


**Fig. 1:** Experiment diagram. (a) The atoms are trapped in a 3D MOT, where the PGC assisted by optical lattice can be achieved through controlling the experimental parameters such as magnetic field, laser power and detuning. The 1-dimension optical lattice is formed by two red detuning laser beams, with intensity distribution following Gaussian and harmonic profile along the radial and axial directions respectively. The atoms are localized at the peak of lattice light. (b) After being released in the vacuum chamber, the atom cloud would reach towards detection zone, generating a TOF signal that can be utilized to calculate the objective function. Each pairwise objective function and corresponding parameters constitutes an observed data point which will be employed for training the Bayesian model. A host computer executes the MHCS-BO algorithm with observed dataset (d), predicting the optimal parameters which are utilized in the laser system through the controller (c).

In this study, we demonstrate a scheme of polarization gradient cooling assisted by optical lattice based on improved BO. Different from existent AI technology used in quantum experiments, we propose the Maximum Hypersphere Compensation Sampling Bayesian Optimization (MHCS-BO). It is illustrated that MHCS-BO has twice optimization efficiency and higher prediction accuracy than traditional Bayesian optimization. As a result, lower atomic temperature and more sufficient atoms can be obtained. In the experiment, the cooling process is divided into 10 segments to be finely controlled, and thus a total of 16 experimental parameters is optimized in a decoupled manner by MHCS-BO. Approximate  $10^8$  cold atoms at a temperature of  $0.4 \pm 0.2 \mu\text{K}$  can be obtained with 15 minutes of MHCS-BO.

## Results

### Experiment setup

The experiment setup is mainly composed of laser systems (see the Supplementary Materials), vacuum chamber, and controller (Fig. 1). Setting reasonable parameters  $X$ , one

experiment cycle can be conducted following the timing sequence depicted in Fig. 2. Consequently, the time-of-flight (TOF) signal can be obtained on the host computer. The atomic temperature  $T_a$  is acquired by fitting TOF signal in velocity domain, which is subsequently used to calculate the objective function  $O(\mathbf{X})$ . A pairwise observed data point consisting of scaled parameters  $\mathbf{X}$  and corresponding  $O(\mathbf{X})$  would be used to fit the surrogate model, which is Gaussian process in this study. MHCS-BO is utilized to predict the optimal parameters for next experiment cycle. The above process iterates until reaching the termination criterion. To finely control the process of PGC, we discarded the linear changing of cooling light parameters in traditional PGC (blue line in Fig. 2). Instead, the PGC interaction time is divided into 10 steps, and each step  $t_i$  ( $i = 1, 2, \dots, 10$ ) is variable to be optimized. The initial power and detuning of cooling light in PGC are the same as that in MOT. There is a time delay  $t_m$  between MOT and PGC. Through adjusting  $t_i$ ,  $P_c$  and  $\delta_c$ , the power and detuning can have different sequence, achieving finely controlling of PGC process. After the completion of PGC, only the lattice light continues to hold on for a certain time  $t_h$  and then unload adiabatically within time  $t_u$  to achieving lower  $T_a$ . However, if  $t_h$  is too long, atoms will be accelerated due to gravity and the lattice, leading to a decrease in the number of atoms in the potential well. Additionally, the power of lattice light  $P_L$  can affect the well depth and scattering rate. A deep well results in more confined atoms, but the velocity distribution of atoms will be widened, increasing the atomic temperature. Conversely, a shallow well corresponds to fewer atom numbers and lower  $T_a$ . Moreover, a higher the scattering rate, which means a higher probability of interaction between atoms and photons, would elevate the probability of atom heating. Thus,  $t_h$  and  $P_L$  are key parameters that needs to be optimized and balanced.

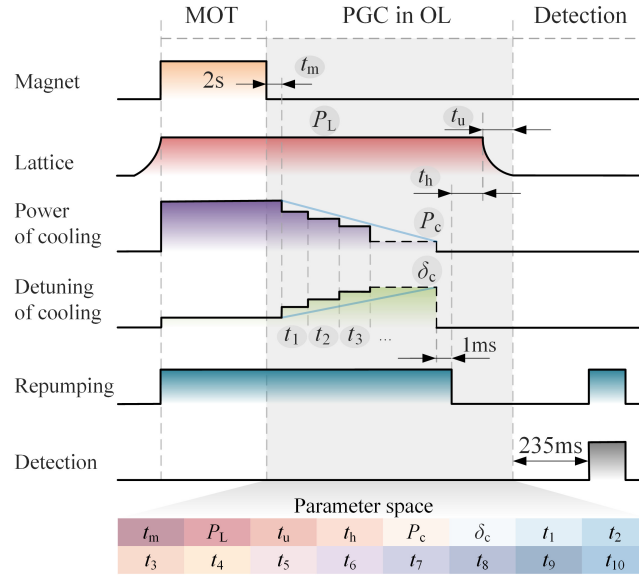


**Fig. 2:** Timing sequence and parameters space. OL, optical lattice;  $t_m$ , time to turn off magnetic coils;  $P_L$ , power of lattice light;  $t_u$ , duration of the optical lattice unloading;  $t_h$ , holding time of optical lattice;  $P_c$ , power of cooling light at the end of PGC;  $\delta_c$ , detuning of cooling light at the end of PGC;  $t_i$  ( $i = 1, 2, \dots, 10$ ), the time step of PGC. The MOT loads for a duration of 2 seconds, followed by the starting of PGC after a delay of  $t_m$ . The atoms are then pumped to the  $F = 2$  state by turning off the repumping light 1 ms later than the cooling light. After being released from lattice, the atoms undergo a 235 ms free-falling in vacuum chamber before reaching the detection zone.

In summary, the parameters that need optimization are  $\mathbf{X}_0 = \{P_c, \delta_c, t_i, t_m, t_u, t_h, P_L\}$  (16 dimensions). As  $P_c$  is controlled by an acousto-optic modulator (AOM), its value can be

directly controlled by setting the attenuation ( $Att$ ) of radio-frequency signal. The  $P_L$  is controlled by another AOM with its radio-frequency signal provided by an arbitrary waveform generator, and the signal amplitude is modulated by the voltage  $V_L$  provided by the controller. We use  $Att$  and  $V_L$  to replace  $P_c$  and  $P_L$  with their relationship detailed in the Supplementary Materials. Therefore, the actual parameters for optimization are  $\{Att, \delta_c, t_i, t_m, t_u, t_h, V_L\}$ . If all parameters are optimized together in a coupled manner, it can easily lead to poor signals (Fig. 5e), misleading the optimization direction. Hence, we first turn off the optical lattice and optimize the PGC-related parameters  $X_p = \{Att, \delta_c, t_i, t_m\}$  to initially cool the atoms to below  $5 \mu\text{K}$ . Subsequently, we turn on the lattice and optimize the lattice-related parameters  $X_L = \{t_m, t_u, t_h, V_L\}$  to achieve a high-quality cold atom cloud. It is noteworthy that the magnetic field delay parameter  $t_m$  also has some impact on the cooling effect in optical lattice, thus it is included in  $X_L$ . The units for the attenuation coefficient, light power, time, and voltage among the aforementioned parameters are dB, mW, ms, and V, respectively.

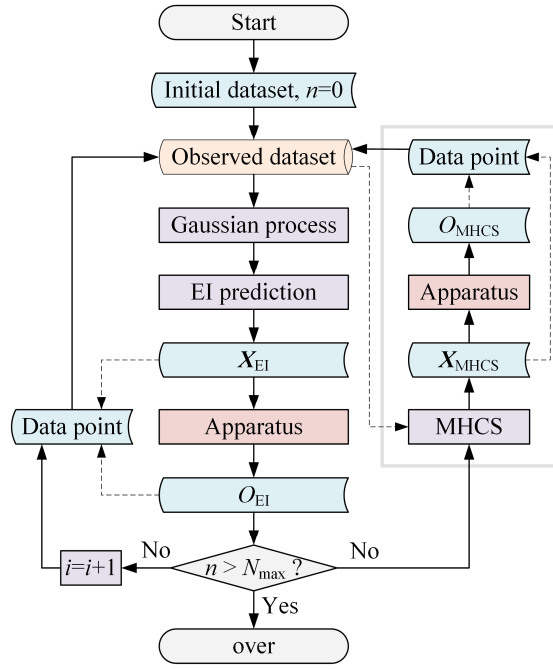


**Fig. 3:** Flowchart of MHCS-BO. The light blue blocks represent the data generated during optimization process, the red blocks indicate implementing parameters to apparatus and conducting one experiment, the purple blocks depict critical steps in BO, and the gray frame indicates MHCH prediction.

MHCS-BO is proposed to find the optimal parameters as shown in Fig. 3. The Gaussian process is fitted initially by the dataset which could be obtained by prior data or randomly sampled in parameter space. The prediction stage is mainly composed of two steps: (1) prediction based on EI function; (2) prediction based on MHCS. The corresponding optimal point  $X_{EI}$  and  $X_{MHCS}$  would be implemented in the apparatus, yielding the objective function  $O_{EI}$  and  $O_{MHCS}$  respectively, all of which would be added to the observed dataset. To balance atomic temperature  $T_a$  and atom number  $N_a$ , the objective function is defined as  $O(\mathbf{X}) = T_a / A_s^b$ , where  $A_s \propto N_a$  represents the amplitude of TOF signal, and  $b$  is a balancing coefficient within range of 0.1-1. As the iteration process running, the fitted Gaussian process would be more accurate to reflect the mapping relationship between the experimental parameters and the corresponding  $O(\mathbf{X})$ . More details can be seen in the Methods section. To assess the performance and generalizability of MHCS-BO, we apply it to 5 standard test functions (29).



The findings reveal that MHCS-BO outperforms traditional BO, with nearly double optimization speed (Fig. 4a) and superior prediction accuracy (Fig. 4b). More details are available in the Supplementary Materials.

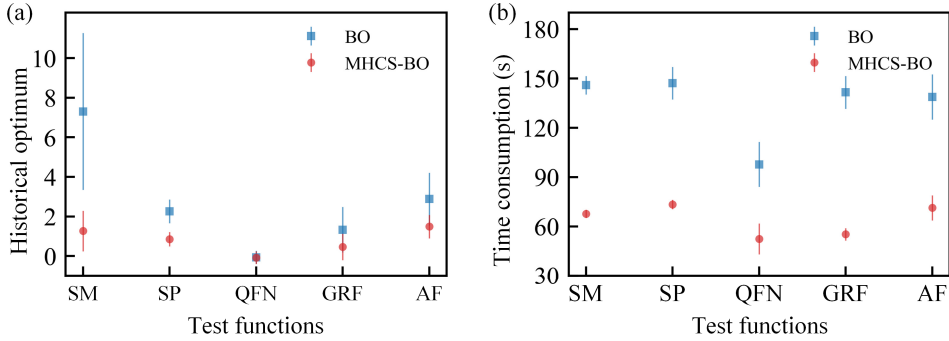


**Fig. 4:** Performance comparison between MHCS-BO and BO under 5 typical test functions. The historical optimum (a) and time consumption (b) under different test functions are displayed. Each data is averaged by 9 repetitions, and the error bars indicate the standard deviation. SM, Sphere Model; SP, Schwefel’s Problem 2.21; QFN, Quartic Function i.e. Noise; GRF, Generalized Rastrigin’s Function; AF, Ackley’s Function.

### Optimization Results

Here, we visually compare the optimization efficiency of MHCS-BO, manual optimization (MO), and grid brute-force search for the 16 parameters in our experiment. MHCS-BO requires decoupling and optimizing the parameters step by step, running a total of 200 experiments, taking about 15 minutes. Even MO is operated by an experienced operator familiar with the system, it typically takes 4-6 hours to obtain satisfactory results. In the context of grid brute-force search, employing a parameter step size of  $P_{\text{range}}/3$  ( $P_{\text{range}}$  is the parameter range), which denotes a coarse granularity, necessitates conducting an impractical number of  $3^{16}$  experiments, equivalent to an estimated duration of approximately 6 years. As a result, MHCS-BO is appropriate to our experiment.

The optimization results under different conditions are illustrated in Fig. 5. The impact of BO and MHCS-BO on the optimization process of PGC is compared (Fig. 5a). It can be observed that in the vast majority of iterative episodes, the EI prediction line in MHCS-BO is significantly lower than that in BO, indicating that MHCS-BO can obtain promising parameters. This implies that exploration of non-sampling sparse regions by the MHCS effectively enhances the completeness of observed dataset, bringing a more precise mapping from the model to apparatus, result in greatly improving EI prediction performance. MHCS-BO and BO reach the historical global optimum at the 61st and 66th episode respectively.

The historical global optimal parameters for MHCS-BO are  $\mathbf{X}_P^* = \{31.5, 188.21, 10.0, 6.42, 2.37, 5.25, 0.9, 0.42, 9.96, 7.76, 1.04, 0.3, 6.87\}$ . Setting the PGC parameters  $\mathbf{X}_P = \mathbf{X}_P^*$ ,  $\mathbf{X}_L$  is optimized keeping the lattice light holding on (Fig. 5b). Similar to Fig. 5a, the majority of the best values are generated by EI predictions. This suggests that MHCS predictions serve as effective supplements to EI predictions, which plays a role to explore the blind areas in the parameter space, thereby enhance the overall performance of the model. However, there is still one MHCS prediction point appearing in the historical best value (gray solid line in Fig. 5b), indicating that the MHCS algorithm has a certain probability of exploring potential optimal values that the EI algorithm cannot predict, highlighting the necessity of the MHCS algorithm. The entire iterative process reaches the historical global

optimum at the 63nd episode with  $X^*_L = \{4.75, 9.76, 0.6, 4.16\}$ . It is noteworthy that the magnetic field delay  $t_m$  here is different from that in  $X^*_P$ , changing from 6.87 ms to 9.67 ms. The overall optimal parameters  $X^* = X^*_P(1:12) \cup X^*_L$ .

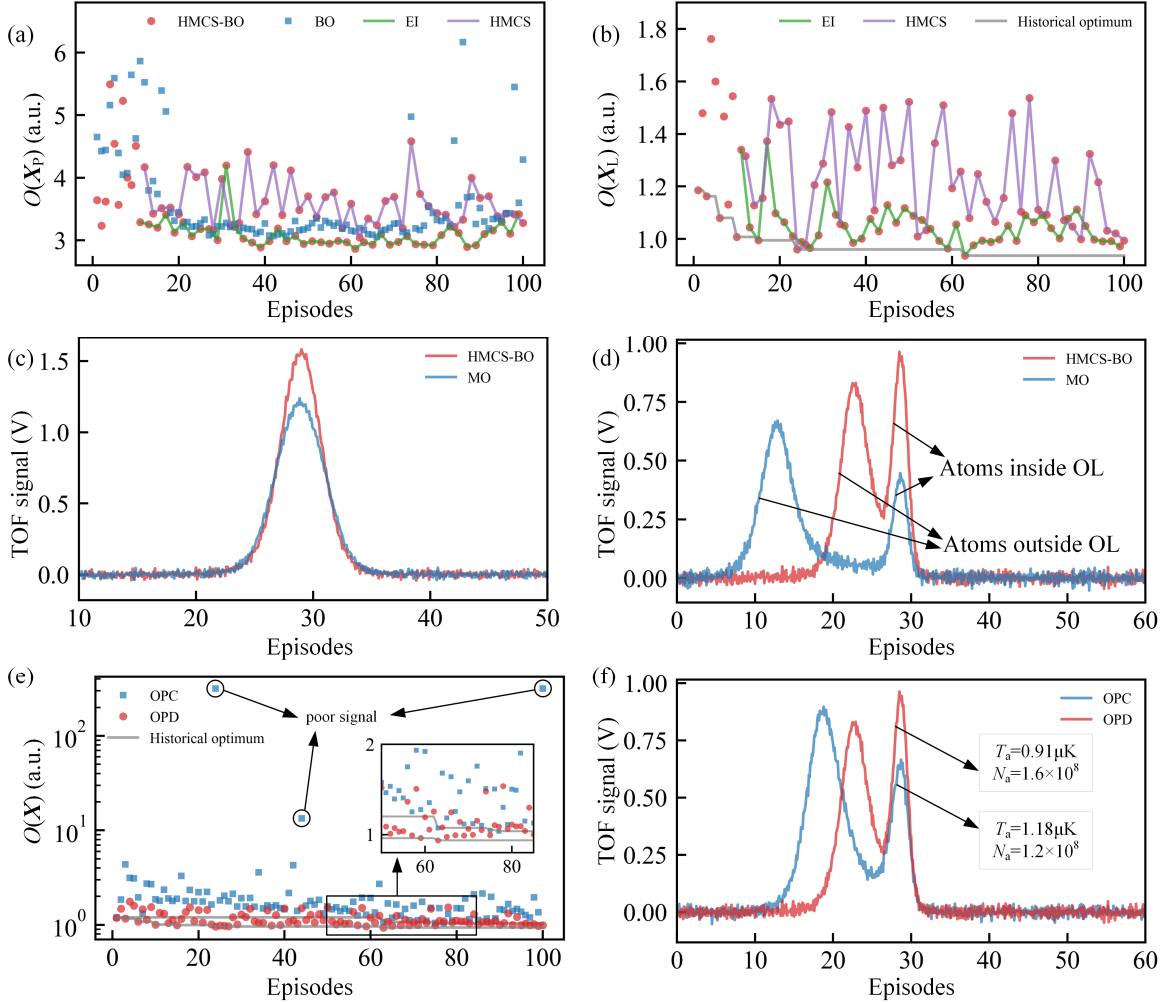


**Fig. 5:** Optimization of PGC and optical lattice. (a) The optimization of PGC using two different BO algorithms, where the blue squares and red dots line represent the BO and MHCS-BO respectively. The purple and green line denotes the EI prediction and MHCS prediction in MHCS-BO. The first 10 points were the initial data obtained through random sampling. (b) The MHCS-BO is used to optimize the 4 parameters of optical lattice, where the purple and green line denotes the EI prediction and MHCS respectively, and the gray solid line represents the historical best value. (c) and (d) show the TOF signals of cold atomic clouds under the optimal parameters when optical lattice is closed and open respectively. (e) The BO process under OPC and OPD conditions, where the gray lines represent their respective historical best values. (f) The best optimization results under OPC and OPD conditions.

The optimal  $T_a$  and  $N_a$  of PGC obtained by MHCS-BO and MO are  $3.1\ \mu\text{K}$ ,  $4.3\ \mu\text{K}$ , and  $4.2\times 10^8$ ,  $3.6\times 10^8$  (Fig. 5c), respectively. Although MO can also achieve a relatively acceptable temperature and atom number, the optimization process relies on the intuition and familiarity of the system. In other words, different individuals may obtain different optimization results, leading to a degree of subjectivity. In contrast, MHCS-BO executes optimization more objectively and accurately based on  $O(X)$ , resulting in significantly higher optimization metrics compared to MO. With optical lattice holding on and the parameters setting to  $X^*$ , the TOF signals of is compared between MHCS-BO and MO (Fig. 5d). It can be seen that due to the dipole trap of optical lattice overcoming some of the effects from gravity, the atoms inside optical lattice fall later than those outside.

Consequently, the peak of TOF signal exhibits a relative lag. Moreover, the TOF signal for atoms confined within optical lattice displays significantly narrower width, indicating a better cooling effect. The optimal  $T_a$  and  $N_a$  inside optical lattice for MHCS-BO and MO are  $0.91 \mu\text{K}$ ,  $0.82 \mu\text{K}$ , and  $1.6 \times 10^8$  and  $7.1 \times 10^7$ , respectively. With the assistance of optical lattice, MO also achieves acceptable atomic temperature, but the atom number is lower than that of MHCS-BO. This is because we have set a comprehensive optimization metric that balances both the atom number and atomic temperature, rather than solely optimizing the atomic temperature.

In order to verify the necessity of parameters decoupling, we compare the optimization under parameters coupling (OPC) and decoupling (OPD) (Fig. 5e). Overall,  $O(\mathbf{X})$  of OPC is generally worse than that of OPD. In our experiments,  $T_a$  cannot be calculated if TOF signal is poor (red circle). In such instance, it is directly assigned the value of 100. As a result, the mapping accuracy between the model and apparatus may be compromised, potentially misleading the optimization direction and slowing down the optimization efficiency. It can be seen that a few poor TOF signals are generated in some episodes under OPC. Conversely, such signal cannot be found in OPD. The optimal  $T_a$  and  $N_a$  inside optical lattice from MO are  $1.18 \mu\text{K}$  and  $7.1 \times 10^7$  respectively (Fig. 5f), even worse than the ones from MO by OPD. Additionally,  $O(\mathbf{X})$  in OPC fluctuates more significantly than OPD, indicating more susceptible to the environment. Therefore, the overall performance of OPD surpasses that of OPC.

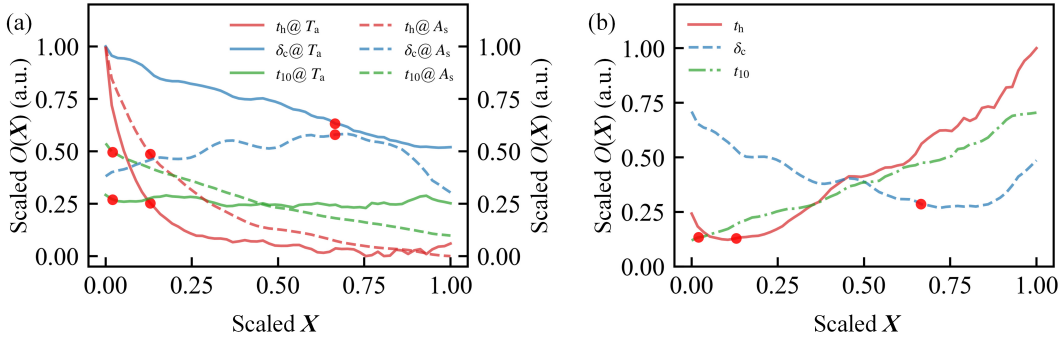


**Fig. 6. Key parameter scans under optimal settings.** (a) The variation of  $T_a$  (solid line) and  $A_s$  (dashed line) with parameter changes. For comprehensive comparison of the experimental effects, the ranges of parameters and their corresponding  $T_a$  and  $A_s$  have been scaled. When each parameter changes, the remaining parameters are kept at the optimum  $\mathbf{X}^*$ , indicated by red dots. (b) The variation of the objective function with each parameter. Each data represents the average of 3 measurements (refer to Supplementary Materials) and has undergone moving average to further suppress measurement noise.

Considering the existence of systemic error and random error, the actual experimental parameters may deviate from the setting value. Therefore, it is crucial to ensure that our experimental results, generated by optimal parameters with a few deviations, are proximal to the optimum. Each parameter is scanned under the optimum ( $\mathbf{X}^*$ ). Here, only the three parameters that have the greatest impact on cooling effects are analyzed as shown in Fig. 6. The results for other parameters can be seen in the Supplementary Materials. As the holding time  $t_h$  increases, both  $T_a$  and  $N_a$  decrease (red line in Fig. 6a). This phenomenon aligns with physical intuition, because the dipole force, scattering force, and gravity all act on the atoms within optical lattice. As a result, some atoms escape from the potential well, leading to a decrease in the number of atoms inside the trap. The remaining atoms are those with kinetic energy less than well depth, which meaning a lower atomic temperature. With the further extension of  $t_h$ ,  $T_a$  will gradually stabilize. When  $\delta_c$  gradually increases (blue line), there is

no apparent pattern in the changes of  $T_a$  and  $A_s$ . Overall, when  $\delta_c$  is not too large,  $T_a$  decreases with increasing  $\delta_c$ , while  $A_s$  exhibits the opposite trend.  $t_{10}$  represents the final time step of PGC. As this value increases,  $A_s$  decreases gradually, while the change in  $T_a$  is less pronounced (green line). This phenomenon indicates that the atoms have already been sufficiently cooled in the preceding time steps. Therefore, extending the value of  $t_{10}$  is equivalent to increasing  $t_h$ , resulting in a corresponding alignment between the trends in  $T_a$  and  $A_s$  with the analysis of  $t_h$ . Since  $O(\mathbf{X})$  is based on  $T_a$  and  $A_s$ , the lowest atomic temperature was not set as the optimization target. Instead, a balance between them was considered. The position of optimal parameter can vividly reflect this, indicating that the objective function has achieved the intended purpose. The changes of  $O(\mathbf{X})$  in the vicinity of the optimal point (Fig. 6b) are relatively smooth, without abrupt gradient shifts. This implies that the optimal parameters  $\mathbf{X}^*$  predicted by MHCS-BO do not coincidentally fall on a singular optimal point and demonstrate a certain degree of robustness, highlighting the superiority of the algorithm proposed in this paper for optimizing multiple parameters in PGC.

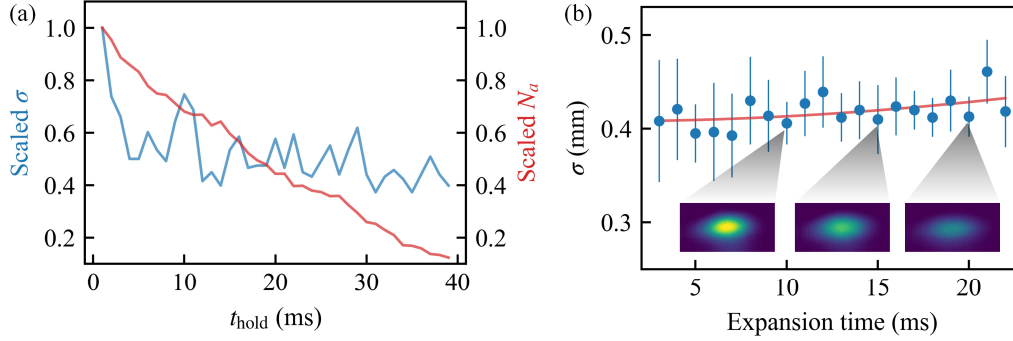


**Fig. 7. Atom temperature test.** (a) scaled  $\sigma$  and  $N_a$  versus  $t_h$ .  $\sigma$  is the Gaussian radii of the atom cloud, which is obtained by fitting the fluorescence image along vertical direction. A smaller  $\sigma$  means a corresponding lower atomic temperature.  $N_a$  is calculated by integrating the counts of fluorescence image. (b) Mean radii of atom cloud versus expansion time. Each data is averaged by 10 repetitions, and the error bars indicate the standard deviation. The insets are fluorescence images of atom cloud taken during ballistic expansion. The loading time is adjusted to 3 seconds in order to enhance the detection signal, while the exposure time of CCD camera is set at 0.5 ms.

In order to further explore lower atomic temperatures, we increase  $t_h$  under the optimal parameters obtained from MHCS-BO. However, as  $t_h$  increased, the number of atoms gradually decreased. Consequently, the atomic fluorescence signal became extremely weak, leading bad TOF signal. Therefore, we increase the MOT loading time to 3 seconds to obtain more atoms, and employ the ballistic expansion method to precisely measure atomic temperature. By setting  $t_h$  to 20 ms, a lower atomic temperature could be achieved without a significant decrease in  $N_a$  (Fig. 7a). Under this condition, images of atom cloud at different expansion time  $t$  were captured by a CCD camera (Fig. 7b), and the following relationship exists between the radius of atom cloud  $\sigma$  and expansion time  $t$  (30).

$$\sigma^2 = \sigma_0^2 + \frac{k_B T_a}{m} t^2 \quad (1)$$

Where  $\sigma_0$  is the initial radius of the atom cloud,  $k_B$  is the Boltzmann constant, and  $m$  is the mass of an  $^{87}\text{Rb}$  atom. By fitting Eq.1, the value of  $T_a$  can be obtained as  $0.4 \pm 0.2 \mu\text{K}$ , a temperature close to the recoil temperature of  $^{87}\text{Rb}$ .

## Discussion

In summary, we have provided the first demonstration of MHCS-BO used in preparing sub- $\mu\text{K}$  cold atoms through PGC assisted with optical lattice. MHCS-BO inherits merit of BO, enhances the prediction accuracy and accelerates experimental parameters optimization. Compared to BO, MO, and grid brute-force search, MHCS-BO exhibits significant superiority in fast predicting optimal experimental parameters. Within 15 minutes of optimization, the final temperature is  $0.4 \pm 0.2 \mu\text{K}$  and the number of atoms after cooling is about  $10^8$ . For the first time, hundreds of millions of cold atoms close to recoil temperature are created, and it can be extended to 3-dimension cooling by adding another lattice beam. One limitation of MHCS-BO however is that it cannot find the complete Pareto frontier in multi-objective optimization problems. Thus, future iteration could use multi-objective BO to overcome this limitation. Overall, this study demonstrates a new scheme to generate high quality sub- $\mu\text{K}$  cold atoms, providing insights for initial cooling of cold atom experiments, e.g., BEC, quantum computing and quantum simulation.

## Methods

### The MOT Configuration

The 3D MOT, as described in our previous work (31), mainly consists of with three mutually orthogonal cooling beams and a pair of anti-Helmholtz coils. The cooling beam has a radius of about 26 mm, a power of about 14mW, and is red-detuned by 15 MHz from  $F = 2 \rightarrow F' = 3$  transition. A Gaussian beam with power of about 30 mW, red detuning of approximately 67 GHz from  $F = 2 \rightarrow F' = 3$  transition, and diameter of around 1.8 mm (forming potential well with depth about  $15\text{-}30T_r$ , where  $T_r \approx 0.362 \mu\text{K}$  is the recoil temperature), is incident into the vacuum chamber, reflected by a mirror to form a 1-dimension optical lattice at the center of the MOT. A CCD camera is mainly used to observe the atom cloud during operation and measure the atomic temperature. The TOF light (about  $72 \mu\text{W}$ ), shaped by a  $100 \text{ mm} \times 1 \text{ mm}$  aperture, and forms the detection region. When the atom cloud passes through this region, the TOF signal is detected by a photonic detector (PD) and conveyed to the host computer by a 16-bit data acquisition card.  $T_a$  and  $N_a$  for this experiment cycle can be obtained by fitting the signal, allowing the calculation of the pre-designed objective function.

### MHCS-BO

Initially, 10 random samples are taken in the parameter space to conduct experiment cycle successively. After calculating the corresponding  $O(\mathbf{X})$ , the initial observed dataset is obtained, which is then used to perform an initial fitting for the Gaussian process. To avoid overfitting, enhance generalization capability, and accelerate convergence, a variable-length adaptive radial basis function kernel is employed as the kernel function, with an initial length of 0.01, varying from 0.001 to 5. The adaptive kernel function can automatically adjust its shape based on the data characteristics, thus flexibly adapting to changes in different data distributions and features. Based on this model, the average value  $\mu$  and standard deviation  $\delta$  at  $\mathbf{X}_s$ , a point sampled in parameter space, can be calculated by:

$$\begin{cases} \mu = K(\mathbf{X}_s, \mathbf{X}_o)[K(\mathbf{X}_o, \mathbf{X}_o) - \sigma_0^2 \mathbf{I}]^{-1} \mathbf{Y}_o \\ \sigma = K(\mathbf{X}_s, \mathbf{X}_s) - K(\mathbf{X}_s, \mathbf{X}_o)[K(\mathbf{X}_o, \mathbf{X}_o) - \sigma_0^2 \mathbf{I}]^{-1} K(\mathbf{X}_o, \mathbf{X}_s) \end{cases} \quad (2)$$

Where  $\mathbf{X}_o = \{\mathbf{X}_1, \mathbf{X}_2, \dots, \mathbf{X}_N\}$ ,  $\mathbf{Y}_o = \{y_1, y_2, \dots, y_N\}^T$  represent the parameter vector and objective function corresponding to each data point,  $\mathbf{K}(\mathbf{X}, \mathbf{Y})_{i,j} = k(\mathbf{X}_i, \mathbf{Y}_j)$  is the covariance

matrix, where  $k(\mathbf{X}_i, \mathbf{Y}_j)$  is the radial basis function kernel between point  $\mathbf{X}_i$  and  $\mathbf{Y}_j$ . The corresponding EI value for  $\mathbf{X}_s$  can be computed as follows:

$$y_{\text{EI}} = \begin{cases} (\mu - y^*)\Phi(z) & \sigma \neq 0 \\ 0 & \sigma = 0 \end{cases} \quad (3)$$

Where  $z = (\mu - y^*)/\sigma$ , and  $y^*$  is the best objective function in observed dataset,  $\Phi(z)$  represents the values of the standard normal distribution at  $z$ . The L-BFGS-B optimization algorithm is utilized to find the maximum value. To avoid getting trapped in local optimum, 30 parameters are randomly selected in the search space as the initial values for L-BFGS-B. Then, the 30 individual optimizations are performed separately. The maximum value among all results is taken as the final optimization result, with the corresponding parameters  $\mathbf{X}_{\text{EI}}$  being the optimal parameters predicted by EI, which is then applied in running one experiment cycle to calculate the objective function  $O_{\text{EI}}$ . The scaled data point  $\{\mathbf{X}_{\text{EI}}, O_{\text{EI}}\}$  is then added to the observed dataset. The MHCS algorithm is used to predicate another data point  $\{\mathbf{X}_{\text{MHCS}}, O_{\text{MHCS}}\}$ , which is also incorporated into the observed dataset. This iterative process continues until the number of iterations reaches the designated maximum iteration steps.

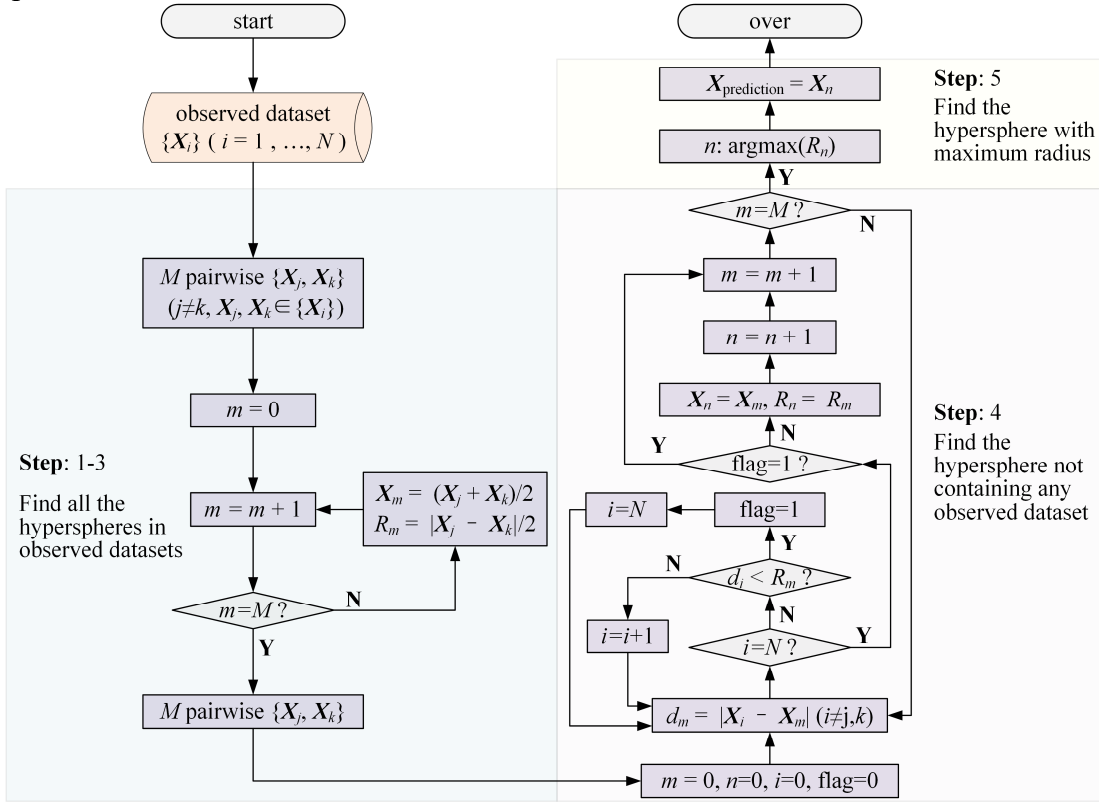


**Fig. 8:** Flowchart of MHCS algorithm. Yellow block represents the observation dataset, light purple blocks represent the parameters, and gray ones represent the key processes.

### MHCS Algorithm

In the traditional BO using EI prediction, the predicated optimal points may cluster in some certain regions, leaving large non-sampling regions. This situation is quite common in high-dimensional spaces, leading to incomplete observation. Consequently, the inaccurate mapping from surrogate model to apparatus reduces the algorithm's performance. The core idea of MHCS is to identify the largest sparse region based on the current observed dataset and sample one point within that region.



Here, we first give a brief introduction to the concept of hypersphere. Assuming that there are two points in the 2-dimensional space,  $\mathbf{X}_1$  and  $\mathbf{X}_2$ , then a circle can be generated with the line connecting the two points as diameter. When the space is expanded to 3 dimensions, this circle turns into a sphere. Similarly, in spaces with more than 3 dimensions as the problem in this study, the sphere becomes a hypersphere. Now we will give a more rigorous mathematical description of the hypersphere. The midpoint between  $\mathbf{X}_1$  and  $\mathbf{X}_2$  is defined as  $\mathbf{X}_c = (\mathbf{X}_1 + \mathbf{X}_2)/2$ . The Euclidean distance between them is denoted as  $D = |\mathbf{X}_1 - \mathbf{X}_2|$ . The surface in the entire parameter space composed of points equidistant from the midpoint at a distance of  $D/2$  is called a hypersphere with  $\mathbf{X}_c$  as the center and a diameter of  $D$ .

The main steps of MHCS algorithm are as follows (Fig. 8):

**Step1:** To ensure consistency across scales for subsequent processing, all observed data points are scaled within the range of 0 to 1.

**Step2:** For the current set of observed  $N$  data points,  $\mathbf{X}_i$  ( $i=0, 1, \dots, N-1$ ), identify all possible pairwise combinations  $\{\mathbf{X}_j, \mathbf{X}_k\}$  ( $j \neq k, \mathbf{X}_j, \mathbf{X}_k \in \{\mathbf{X}_i\}$ ).

**Step3:** Calculate their respective centers  $\{\mathbf{X}_c\}$  and radius  $\{R_c\}$ , where  $c = 0, 1, \dots, M$ .

**Step4:** For each combination  $\{\mathbf{X}_j, \mathbf{X}_k\}$  corresponding to a hypersphere, iterate through all observed parameters  $\{\mathbf{X}_i\}$  ( $i \neq j, k$ ). If any observed parameter satisfies  $|\mathbf{X}_c - \mathbf{X}_i| < R_c$ , it indicates that there is no observed data point is within this hypersphere, which is then selected as a candidate hypersphere.

**Step5:** Choose the candidate hypersphere with the largest radius, and the corresponding center  $\mathbf{X}_c$  is the recommended point of the algorithm.

## References and Notes

1. Peters, K. Y. Chung, S. Chu, Measurement of Gravitational Acceleration by Dropping Atoms. *Nature*. **400** (6747), 849–852 (1999).
2. K. M. Jones, E. Tiesinga, P. D. Lett, P. S. Julienne, Ultracold photoassociation spectroscopy: Long-range molecules and atomic scattering. *Rev. Mod. Phys.* **78** (2), 483–535 (2006).
3. M. S. Safronova, D. Budker, D. DeMille, D. F. J. Kimball, A. Derevianko, C. W. Clark, Search for new physics with atoms and molecules. *Rev. Mod. Phys.* **90** (2), 025008 (2018).
4. V. Cimini, M. Valeri, E. Polino, S. Piacentini, F. Ceccarelli, G. Corrielli, N. Spagnolo, R. Osellame, F. Sciarrino, Deep Reinforcement Learning for Quantum Multiparameter Estimation. *Adv. Photonics* **5** (1), 016005 (2023).
5. A. N. Ciavarella, S. Caspar, H. Singh, M. J. Savage, Preparation for quantum simulation of the  $(1 + 1)$ -dimensional  $O(3)$  nonlinear  $\sigma$  model using cold atoms. *Phys. Rev. A* **107** (4), 042404 (2023).
6. R. Ott, T. V. Zache, F. Jendrzejewski, J. Berges, Scalable Cold-Atom Quantum Simulator for Two-Dimensional QED. *Phys. Rev. Lett.* **127** (13), 130504 (2021).
7. J. C. Halimeh, I. P. McCulloch, B. Yang, P. Hauke, Tuning the Topological  $\theta$ -Angle in Cold-Atom Quantum Simulators of Gauge Theories. *PRX Quantum* **3** (4), 040316 (2022).
8. A. Cao, W. J. Eckner, T. L. Yelin, A. W. Young, S. Jandura, L. Yan, K. Kim, G. Pupillo, J. Ye, N. D. O’ppong, A. M. Kaufman, Multi-qubit gates and Schrödinger cat states in an optical clock. *Nature*. **634** (8033), 315–320 (2024).
9. J.-M. Mol, L. Esguerra, M. Meister, D. E. Bruschi, A. W. Schell, J. Wolters, L. Wörner, Quantum Memories for Fundamental Science in Space. *Quantum Sci. Technol.* **8** (2), 024006 (2023).
10. I. V. Vovchenko, V. Yu. Shishkov, E. S. Andrianov, Dephasing-Assisted Entanglement in a System of Strongly Coupled Qubits. *Opt. Express* **29** (6), 9685 (2021).
11. M. Kasevich, S. Chu, Atomic Interferometry Using Stimulated Raman Transitions. *Phys. Rev. Lett.* **67** (2), 181–184 (1991).
12. S. Ejtemaee, P. C. Haljan, 3D Sisyphus Cooling of Trapped Ions. *Phys. Rev. Lett.* **119** (4), 043001 (2017).
13. Y. Wang, Y. Li, J. Wu, W. Liu, J. Hu, J. Ma, L. Xiao, S. Jia, Hybrid Evaporative Cooling of  $^{133}\text{Cs}$  Atoms to Bose-Einstein Condensation. *Opt. Express* **29** (9), 13960–13967 (2021).
14. E. Zohar, Y. Florshaim, O. Zilberman, A. Stern, Y. Sagi, Degenerate Raman Sideband Cooling of 40K Atoms. *Phys. Rev. A* **106** (6), 063111 (2022).
15. C. Wei, C. C. N. Kuhn, Laser Cooling of Rubidium Atoms in a 2D Optical Lattice. *J. Mod. Opt.* **65** (10), 1226–1234 (2018).
16. P. B. Wigley, P. J. Everitt, A. van den Hengel, J. W. Bastian, M. A. Sooriyabandara, G. D. McDonald, K. S. Hardman, C. D. Quinlivan, P. Manju, C. C. N. Kuhn, I. R. Petersen, A. N. Luiten, J. J. Hope, N. P. Robins, M. R. Hush, Fast Machine-Learning Online Optimization of Ultra-Cold-Atom Experiments. *Sci. Rep.* **6** (1), 25890 (2016).
17. G. Carleo, M. Troyer, Solving the Quantum Many-Body Problem with Artificial Neural Networks. *Science* **355** (6325), 602–606 (2017).

18. G. Torlai, G. Mazzola, J. Carrasquilla, M. Troyer, R. Melko, G. Carleo, Neural- Network Quantum State Tomography. *Nat. Phys.* **14** (5), 447–450 (2018).
19. W. Rohringer, R. Bücker, S. Manz, T. Betz, Ch. Koller, M. Göbel, A. Perrin, J. Schmiedmayer, T. Schumm, Stochastic Optimization of a Cold Atom Experiment Using a Genetic Algorithm. *Appl. Phys. Lett.* **93** (26), 264101 (2008).
20. P. Palittapongarnpim, P. Wittek, E. Zahedinejad, S. Vedaie, B. C. Sanders, Learning in Quantum Control: High-dimensional Global Optimization for Noisy Quantum Dynamics. *Neurocomputing* **268**, 116–126 (2017).
21. H. Che, A. Li, J. Fang, X. Chen, F.-J. Qin, Interference Fringe Fitting of Atom Gravimeter Based on Fitness Particle Swarm Optimization. *AIP Adv.* **12** (7), 075211 (2022).
22. Q. Liu, Y. Xie, L. Li, A. Liang, W. Li, H. Chen, S. Fang, Q. Qu, L. Liu, B. Wang, D. Lü, Multiparameter Autonomous Optimization System for Ultracold Atomic Experiments Based on Artificial Neural Network. *Chin. J. Lasers* **48** (24), 2412001 (2021).
23. A. D. Tranter, H. J. Slatyer, M. R. Hush, A. C. Leung, J. L. Everett, K. V. Paul, P. Vernaz-Gris, P. K. Lam, B. C. Buchler, G. T. Campbell, Multiparameter Optimisation of a Magneto- Optical Trap Using Deep Learning. *Nat. Commun.* **9** (1), 4360 (2018).
24. Z. Vendeiro, J. Ramette, A. Rudelis, M. Chong, J. Sinclair, L. Stewart, A. Urvoy, V. Vuletić, Machine-Learning-Accelerated Bose-Einstein Condensation. *Phys. Rev. Research* **4** (4), 043216 (2022).
25. C. LeDesma, K. Mehling, J. Shao, J. D. Wilson, P. Axelrad, M. M. Nicotra, D. Z. Anderson, M. Holland, Demonstration of a programmable optical lattice atom interferometer. *Phys. Rev. Research* **6** (4), 043120(2024).
26. M. Reinschmidt, J. Fortágh, A. Günther, V. V. Volchkov, Reinforcement Learning in Cold Atom Experiments. *Nat. Commun.* **15** (1), 8532 (2024).
27. A. J. Barker, H. Style, K. Luksch, S. Sunami, D. Garrick, F. Hill, C. J. Foot, E. Bentine, Applying Machine Learning Optimization Methods to the Production of a Quantum Gas. *Mach. Learn.: Sci. Technol* **1** (1), 015007 (2020).
28. S. Xu, P. Kaebert, M. Stepanova, T. Poll, M. Siercke, S. Ospelkaus, Maximizing the Capture Velocity of Molecular Magneto-Optical Traps with Bayesian Optimization. *New J. Phys.* **23** (6), 063062 (2021).
29. X. Yao, Y. Liu, G. Lin, Evolutionary Programming Made Faster. *IEEE Trans. Evolut. Comput.* **3** (2), 82–102 (1999).
30. W. Xin, S. Yuan, Research progress of cold atomic temperature measurement methods. *Chin. J. Sci. Instrum.* **44** (9), 70–82 (2024).
31. C. Liang, S. Gao, J. Liu, G. Wang, S. Yan, J. Yang, L. Zhu, X. Ma, Multi-Parameter Optimization of Polarization Gradient Cooling for  $^{87}\text{Rb}$  Atoms Based on Reinforcement Learning. *Opt. Express* **32** (23), 40364–40374 (2024).

## Acknowledgments

### Funding:

National Natural Science Foundation of China grant 12404556 (X. M.)

National Natural Science Foundation of China grant 62103426 (C. Z.)

**Author contributions:** L. Z., J. Y. and S. Y. conceived the idea. C. L., X. M. and R. S. performed the cold atom experiments. C. L. write the optimization code. S. Y. and J. Y. supervised the program. J. L., C. Z. and G. W. contributed to the scientific discussion. C. L., R. S., and X. M wrote the manuscript with input from all authors.

**Competing interests:** The authors declare that they have no competing interests.

**Data and materials availability:** All data needed to evaluate the conclusions in the paper are present in the paper and/or the Supplementary Materials.